


Impurity effect on Bogoliubov Fermi surfaces: Analysis based on iron-based superconductorsTatsuya Miki,¹ Hiroaki Ikeda², and Shintaro Hoshino¹¹*Department of Physics, Saitama University, Shimo-Okubo, Saitama 338-8570, Japan*²*Department of Physics, Ritsumeikan University, Kusatsu 525-8577, Japan* (Received 10 April 2023; revised 28 August 2023; accepted 29 January 2024; published 4 March 2024)

The effect of impurities on a superconductor with Bogoliubov Fermi surfaces (BFSs) is studied using a realistic tight-binding model. Based on the band structure composed of d -orbitals in tetragonal FeSe, whose S-doped sample is a potential material for a BFS, we construct the superconducting state by introducing a time-reversal broken pair potential in terms of the band index. We further consider the effect of impurities on the BFS, where the impurity potential is defined as a local potential for the original d -orbitals. The self-energy is calculated using the (self-consistent) Born approximation, which shows an enhancement of the single-particle spectral weight on the Fermi surface. This is consistent with the previous phenomenological theory and is justified by the present more detailed calculation based on the FeSe-based material.

DOI: [10.1103/PhysRevB.109.094502](https://doi.org/10.1103/PhysRevB.109.094502)**I. INTRODUCTION**

The phenomenon of superconductivity is induced by Cooper-pair condensation near the Fermi surface, which typically results in the formation of a superconducting gap at the Fermi level. This gap structure is usually classified into three categories: full-gap, point-node, and line-node [1]. However, it has been suggested that some superconductors exhibit a fourth type of gap structure known as a Bogoliubov Fermi surface (BFS) or ultranodal pair, in which the Fermi surface persists even in the superconducting state. This type of superconductor was first proposed in the context of multiband superconductors [2,3] and superfluid helium [4–6]. More recently, specific models with broken time-reversal symmetry and preserved inversion symmetry have also been proposed as candidate systems [7,8]. In these models, the BFS is topologically protected and remains stable against small perturbations. The characteristic features of the BFS have been the subject of theoretical studies [9–30].

In addition to these theoretical studies, the possibility of BFSs has been experimentally implied. It has been pointed out in some materials with unconventional superconductivity that there exists a residual zero-energy density of states (DOS) in the superconducting state [31–34]. Especially in Fe(Se, S), the zero-energy DOS and the presence of low-energy carriers have been observed through the tunnel conductance of scanning tunneling spectroscopy [35], heat capacity, thermal conductivity [36,37], and laser angle-resolved photoemission spectroscopy [38]. As for the theoretical description of the BFS in Fe(Se, S), the interband pairing with broken time-reversal symmetry is suggested to play an important role for the system having the BFS [16]. This model has succeeded in qualitatively reproducing the behavior of the DOS and the heat capacity.

Given the fact that the actual materials may have BFSs, it is interesting to ask if there exists characteristic physics specific to superconductors with BFSs. The electronic states near the BFS are composed of Bogoliubov quasiparticles (bogolons),

which describe the low-energy excitation of the superconducting state. It is expected that the low-energy properties are governed by the bogolon's nature. In our previous work, the authors pointed out that the characteristic feature of a bogolon enters through the impurity scattering and interaction [25]. We studied the physical properties of the Bogoliubov Fermi liquid state near the BFS for a system with preserved inversion and broken time-reversal symmetries, and we found that the pair amplitude (anomalous Green's function) of bogolons becomes finite. Interestingly, the pair amplitude has a purely odd function with respect to the relative time of two bogolons, which is called the odd-frequency pairing. The concept of odd-frequency pairing has been previously examined in relation to electrons and ³He [39–47], but in the present context, the Cooper pair is composed of bogolons. Since the impurity effect gives a dominant contribution at low energies, we analyzed it in detail and found that the odd-frequency pair induces the zero-energy peak in the single-particle DOS in bulk. While this analysis can capture a qualitative feature of the BFS, the origin of the impurity potential on bogolons is not clear, which should be derived from the scattering potential defined in terms of original electrons.

In this paper, we derive the effective low-energy model of bogolons by starting with the tight-binding model of FeSe. We use the realistic tight-binding model of full d -orbitals at the Fe site generated from the first-principles calculation. We then add the intraband and interband pair potentials following Ref. [16] to create the BFS. We further consider the impurity potential defined in the original normal electrons, and we clarify its effect on the bogolons near the BFS. Although these forms of the pair potential are not fully realistic, our approach can estimate the order of magnitude for physical quantities. This work also demonstrates the validity of the phenomenological description of the low-energy physics of the bogolons given in Ref. [25].

This paper is organized as follows. In Sec. II we review the appearance of the odd-frequency pair of bogolons and compare it with the electrons' Cooper pair. Sections III and

	Electron in s-wave SC	(spinless) Bogolon near BFS
Clean	Even-freq. pair	No Cooper pair
Dirty	Even- & Odd-freq. pair	Even- & Odd-freq. pair
Impurity averaged	Even-freq. pair	Odd-freq. pair

FIG. 1. Schematic table for the mechanism of odd-frequency pairing of bogolons and its comparison with the s -wave superconductor. The second row (“Clean”) shows the frequency dependence of the Cooper pairs in the clean limit. The third row (“Dirty”) shows that of the dirty superconductor. The pairs that remain after the impurity average are indicated in the fourth row.

IV are devoted to an explanation of our model of a BFS based on FeSe. In Sec. V, we show the numerical results for the single-particle spectra. We summarize our results in Sec. VI. Below, we take the unit $\hbar = k_B = a = 1$, where a is a lattice constant. Some computational details are provided in Appendices A–D.

II. OVERVIEW: ODD-FREQUENCY PAIRING OF BOGOLONS

Before we go into the details of the tight-binding model study, we provide here an overview of the concept of our work by comparing the two cases: electrons in the conventional (s -wave) superconductor, and low-energy bogolons near the BFS discussed in Refs. [25,26]. We assume that the system with the BFS has inversion symmetry and no time-reversal symmetry. Although the pure odd-frequency pair of bogolons is generally induced by nonideality, i.e., disorder or interaction effects [25], we limit ourselves below to the impurity effect, which becomes dominant at low energies.

As schematically shown in Fig. 1, we consider the two superconducting systems with an impurity potential. In both cases, the total Hamiltonian is given in the form $\mathcal{H} = \mathcal{H}_0 + \mathcal{H}_{\text{imp}}$, where \mathcal{H}_0 is a clean-limit part and \mathcal{H}_{imp} is an impurity potential part. The clean-limit part is explicitly given by $\mathcal{H}_0 = \sum_{k\sigma} (\varepsilon_k c_{k\sigma}^\dagger c_{k\sigma} + \Delta c_{k\uparrow}^\dagger c_{-k,\downarrow}^\dagger + \text{H.c.})$ for electrons with the single-particle energy ε_k , the annihilation operator $c_{k\sigma}$, and the s -wave pair potential Δ (left column). As for the low-energy effective model of bogolons, the Hamiltonian is $\mathcal{H}_0 = \sum_k \varepsilon_k^b \alpha_k^\dagger \alpha_k$, where α_k is the annihilation operator of the bogolon (right column). We note that the latter bogolon model describes the degrees of freedom near the BFS and does not have a spin index and an off-diagonal part since we assume the broken time-reversal symmetry and preserved inversion symmetry [25]. Namely, since Δ_k^b depends only on the wave vector, we have the identity $\sum_k \Delta_k^b \alpha_k^\dagger \alpha_{-k}^\dagger = -\sum_k \Delta_{-k}^b \alpha_k^\dagger \alpha_{-k}^\dagger = 0$ for $\Delta_k^b = \Delta_{-k}^b$. This point is summarized in the second row (labeled as “Clean”) of Fig. 1.

In the presence of impurity potentials, the Green’s functions $\hat{G}_{kk'}$ is written in the form of a 2×2 matrix by using

a Nambu spinor $(c_{k\uparrow}, c_{-k,\downarrow}^\dagger)^T$ for electrons with s -wave superconductivity and $(\alpha_k, \alpha_{-k}^\dagger)^T$ for bogolons near the BFS, respectively. The Green’s functions for each system satisfy the Dyson equation, which is written as

$$\hat{G}_{kk'}(i\omega_n) = \hat{G}_k^0(i\omega_n) \delta_{kk'} + \hat{G}_k^0(i\omega_n) \sum_{k_1} \hat{u}_{kk_1} \hat{G}_{k_1 k'}(i\omega_n), \quad (1)$$

where $\hat{u}_{kk'}$ is an impurity scattering matrix, which is to be averaged. ω_n is a fermionic Matsubara frequency.

One may wonder if the odd-frequency pair amplitude might not arise from the static potential \hat{u}_{kk_1} . The appearance of the dynamical pair amplitude and pair potential can be understood by considering the lowest-order perturbation term. The first-order term vanishes after the random average, and hence we consider the second-order self-energy of the impurity potential:

$$\hat{\Sigma}_{kk'}(i\omega_n) = \sum_{k_1} \hat{u}_{kk_1} \hat{G}_{k_1}^0(i\omega_n) \hat{u}_{k_1 k'}. \quad (2)$$

This self-energy includes both the even- and odd-frequency parts originating from the Green’s function G^0 , and it breaks the inversion and translational symmetry. This situation is summarized in the third row (labeled as “Dirty”) of Fig. 1. After taking an impurity average, the inversion and translational symmetry are recovered (see the fourth row of Fig. 1).

The above Green-function structures are the same between electrons in an s -wave superconductor and bogolons near the BFS. Below, we clarify the difference between the two superconducting systems by focusing on the detailed structures of the Green’s functions.

A. Electrons in an s -wave superconductor

First, we consider the case of the s -wave superconductor with inversion symmetry in the clean limit. The unperturbed Green’s function is given by

$$\hat{G}_k^0(i\omega_n) = \begin{pmatrix} G_k^0(i\omega_n) & F_k^0(i\omega_n) \\ F_k^{0\dagger}(i\omega_n) & \bar{G}_k^0(i\omega_n) \end{pmatrix}. \quad (3)$$

The off-diagonal part is present already in the clean limit. Now we consider the effect of nonmagnetic impurities. Since the impurity scattering potential is gauge-invariant in terms of electrons, $\hat{u}_{kk'}$ has only the diagonal part:

$$\hat{u}_{kk'} = \begin{pmatrix} u(\mathbf{k}, \mathbf{k}') & 0 \\ 0 & -u(\mathbf{k}', \mathbf{k}) \end{pmatrix}. \quad (4)$$

Inserting Eqs. (3) and (4) into Eq. (2), the pair potential $[\hat{\Sigma}_{kk'}(i\omega_n)]_{12}$ can be written as

$$[\hat{\Sigma}_{kk'}(i\omega_n)]_{12} = \sum_{k_1} u(\mathbf{k}, \mathbf{k}_1) F_{k_1}^0(i\omega_n) u(\mathbf{k}_1, \mathbf{k}'). \quad (5)$$

We note that only the spin-singlet pair is induced for a nonmagnetic impurity. The frequency dependence enters through $F_{k_1}^0(i\omega_n)$, which is the even function of frequency. Correspondingly, the pair potential also has the even frequency functional form after the impurity average [see the fourth row (labeled as ‘‘Impurity averaged’’) of Fig. 1].

B. Low-energy bogolons near the Bogoliubov Fermi surface

We consider next the case of a bogolon. In the clean limit, the Green’s function is given by

$$\hat{G}_k^0(i\omega_n) = \begin{pmatrix} G_k^0(i\omega_n) & 0 \\ 0 & \bar{G}_k^0(i\omega_n) \end{pmatrix}, \quad (6)$$

where the inversion symmetry prohibits off-diagonal terms. Since the gauge symmetry is broken, the impurity potential of a bogolon generally has both diagonal ($\alpha^\dagger\alpha$) and off-diagonal ($\alpha^\dagger\alpha^\dagger$) terms effectively, which are denoted by $u_1(\mathbf{k}, \mathbf{k})$ and $u_2(\mathbf{k}, \mathbf{k}')$, respectively. We write the concrete form of $\hat{u}_{kk'}$ as follows:

$$\hat{u}_{kk'} = \begin{pmatrix} u_1(\mathbf{k}, \mathbf{k}') & u_2(\mathbf{k}, \mathbf{k}') \\ u_2(\mathbf{k}', \mathbf{k})^* & -u_1(\mathbf{k}', \mathbf{k}) \end{pmatrix}. \quad (7)$$

The pair potential (=anomalous self-energy) then becomes

$$[\hat{\Sigma}_{kk'}(i\omega_n)]_{12} = \sum_{k_1} [u_1(\mathbf{k}, \mathbf{k}_1) G_{k_1}^0(i\omega_n) u_2(\mathbf{k}_1, \mathbf{k}') + u_2(\mathbf{k}, \mathbf{k}_1) \bar{G}_{k_1}^0(i\omega_n) u_1(\mathbf{k}_1, \mathbf{k}')]. \quad (8)$$

We note that the diagonal Green’s function $G_{k_1}^0(i\omega_n) = 1/(\omega_n - \varepsilon_k^b)$ is composed of mixed even and odd functions of frequency. After taking the impurity average, the inversion and translational symmetry are recovered, i.e., $[\hat{\Sigma}_{kk'}(i\omega_n)]_{12} \propto [\hat{\Sigma}_k(i\omega_n)]_{12} \delta_{kk'}$ with $[\hat{\Sigma}_k(i\omega_n)]_{12} = [\hat{\Sigma}_{-k}(i\omega_n)]_{12}$. In addition, the pair potential obeys the Fermi-Dirac statistics written as $[\hat{\Sigma}_k(i\omega_n)]_{12} = -[\hat{\Sigma}_{-k}(-i\omega_n)]_{12}$. Then, $[\hat{\Sigma}_k(i\omega_n)]_{12}$ becomes the odd function of frequency (the fourth row of Fig. 1). The pure odd-frequency pair of the bogolon is thus realized. We emphasize that the pair is induced by the self-energy of the bogolon and its ω -dependence is purely odd-frequency, which is different from the mixed even- and odd-frequency electrons’ Cooper pair considered in Refs. [27,28]. We note that the interaction effect also induces the self-energies and the odd-frequency pairing amplitude, although the impurity effect is dominant at low-frequency and low-temperature limits [25].

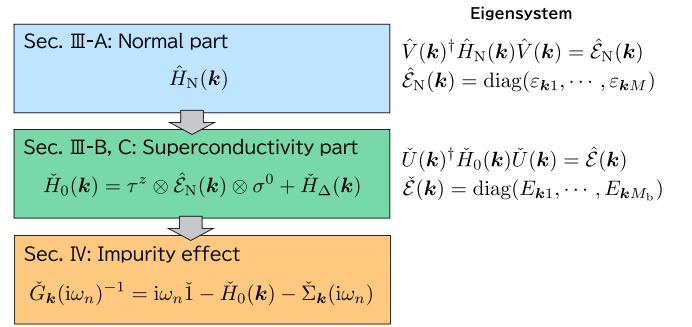


FIG. 2. Flow of the calculation. The normal part is discussed in Sec. III A, while Secs. III B and III C deal with the superconductivity part. We list the notations of the Hamiltonians, the eigenenergies, and vectors for each part as shown in the figure. We discuss the impurity effect in Sec. IV.

In the following sections, in order to clarify the microscopic origin of u_1 and u_2 and their physical consequences, we investigate the impurity effect on the BFS based on the realistic tight-binding model, where the impurity potential is defined in the real-space representation in terms of the original electrons.

III. MODEL HAMILTONIAN AND BOGOLIUBOV FERMI SURFACE

In this section, we introduce a model for BFS. The total Hamiltonian is composed of three parts: $\mathcal{H} = \mathcal{H}_N + \mathcal{H}_\Delta + \mathcal{H}_{\text{imp}}$, where \mathcal{H}_N is a normal state Hamiltonian for the clean limit, \mathcal{H}_Δ is a pair potential part, and \mathcal{H}_{imp} is an impurity potential part. These are discussed, respectively, in Secs. III A, III B, and IV. Since the procedure is complicated, we summarize the calculation flow and notations in Fig. 2.

A. Normal state for the clean limit

Below, we construct the Hamiltonian with the real material Fe(Se, S) in mind. Since the effect of the S-doping is expected to give a chemical pressure, we assume that it does not change the band structure significantly. Accordingly, we use the tight-binding parameters based on the first-principles calculation of FeSe. However, as is well known, the number and size of the experimentally observed Fermi surfaces deviate significantly from the first-principles calculations [48], so we have adjusted their band structure here (see Appendix A for details). Although FeSe has a nematic transition from the tetragonal ($P4/nmm$) phase to the orthorhombic ($Cmma$) phase, we use the hopping parameters for the tetragonal case. This is because the finite zero-energy DOS inside the superconducting phase is observed in the tetragonal phase of Fe(Se, S) experimentally [35–37]. Below, we do not consider the spin-orbit coupling in the normal state for simplicity.

From the band-structure calculation, we can obtain the tight-binding Hamiltonian written by the orthogonal basis of the Wannier function $w_\gamma(\mathbf{r} - \mathbf{R}_n - \mathbf{d}_a)$, where \mathbf{R}_n denotes the center of each unit cell, and \mathbf{d}_a ($a = \text{Fe 1}, \text{Fe 2}$) specifies the position of Fe inside the unit cell measured from \mathbf{R}_n . The atomic orbitals are described by $\gamma = z^2, xz, yz, x^2 - y^2, xy$. See Appendix A for more details about the derivation of tight-

binding model parameters. The normal state Hamiltonian is written by the creation and annihilation operators as

$$\begin{aligned} \mathcal{H}_N = & \sum_{nm} \sum_{aa'\gamma\gamma'\sigma} H_{N\gamma\gamma'}(\mathbf{R}_n + \mathbf{d}_{a'} - \mathbf{d}_a) \\ & \times c_{\gamma\sigma}^\dagger(\mathbf{R}_m + \mathbf{d}_a) c_{\gamma'\sigma}(\mathbf{R}_m + \mathbf{R}_n + \mathbf{d}_{a'}) \\ & - \mu \sum_{na\gamma\sigma} c_{\gamma\sigma}^\dagger(\mathbf{R}_n + \mathbf{d}_a) c_{\gamma\sigma}(\mathbf{R}_n + \mathbf{d}_a). \end{aligned} \quad (9)$$

Since the original parameters have numerical errors, we use the parameters averaged by the symmetry operation as explained in Appendix B.

Performing the Fourier transformations with respect to the lattice vector \mathbf{R}_n , we obtain the Fourier component of the Hamiltonian expressed by $H_{N\gamma, a'\gamma'}(\mathbf{k})$. Then we diagonalize the matrix $H_{N\gamma, a'\gamma'}(\mathbf{k})$ at each \mathbf{k} point, and we calculate the electron band energies numerically. We express this as

$$\begin{aligned} \hat{V}(\mathbf{k})^\dagger \hat{H}_N(\mathbf{k}) \hat{V}(\mathbf{k}) &= \hat{\mathcal{E}}_N(\mathbf{k}) \\ &= \text{diag}(\varepsilon_{k1}, \dots, \varepsilon_{kM}), \end{aligned} \quad (10)$$

where the hat ($\hat{\cdot}$) symbol represents an $M \times M$ matrix, where $M = \sum_{a\gamma} 1 = 10$. Then, we obtain the diagonalized Hamiltonian as

$$\mathcal{H}_N = \sum_{\mathbf{k}} \sum_{\lambda\sigma} (\varepsilon_{k\lambda} - \mu) c_{k\lambda\sigma}^\dagger c_{k\lambda\sigma}, \quad (11)$$

where λ is a band index. The Fermi surfaces in the normal state are shown in Fig. 3(a) with gray solid lines. The two hole pockets appear around the Γ point, and the electron pocket appears around the M point.

To introduce the pair potential in the band basis, we need to identify which bands are connected to each other at different \mathbf{k} points, especially when two bands are crossed. For this identification, we consider the eigenvector $\mathbf{v}(\mathbf{k})_\lambda$ written as

$$\mathbf{v}(\mathbf{k})_\lambda = ([\hat{V}(\mathbf{k})]_{a_1\gamma_1, \lambda}, \dots, [\hat{V}(\mathbf{k})]_{a_M\gamma_M, \lambda})^T. \quad (12)$$

We determine which band (λ') at $\mathbf{k} + \Delta\mathbf{k}$ connects to the band λ at \mathbf{k} by using the inner product of the eigenvectors. Namely, for a given $\mathbf{v}(\mathbf{k})_\lambda$, we choose the index λ' which maximizes the magnitude of $|\mathbf{v}(\mathbf{k} + \Delta\mathbf{k})_{\lambda'} \cdot \mathbf{v}(\mathbf{k})_\lambda|$. Thus we make the band structure smooth for each band index.

B. Pair potential part

Here, we consider the pair potential part phenomenologically, following the procedure given in Ref. [16]. It is important to consider the interband pairing with time-reversal symmetry breaking for BFSs. Below, for convenience of explanation, we assume that the bands with the indices $\lambda = 1, 2, 3, 4$ constitute the normal Fermi surfaces, which are shown in Fig. 3(a) with gray lines. $\lambda = 1, 2$ corresponds to the two Fermi surfaces around the Γ point, where the small one is labeled as $\lambda = 1$ and the large one as $\lambda = 2$. Similarly, $\lambda = 3, 4$ makes the Fermi surfaces around the M point (the curved one at the corner is labeled as $\lambda = 3$, and the straight one as $\lambda = 4$).

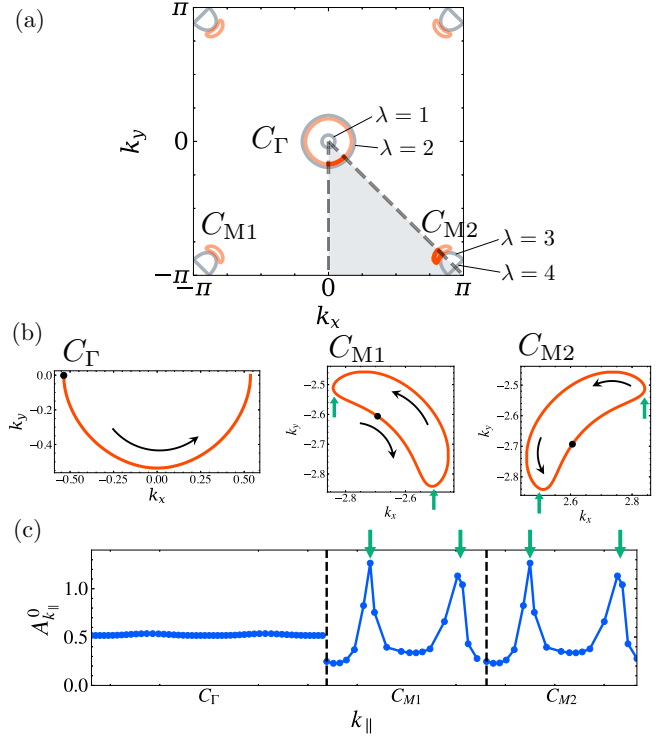


FIG. 3. (a) Normal Fermi surfaces (gray) and BFSs (red). The magnified view of the BFSs is shown in (b). (c) Zero-energy spectral function for the clean limit. The horizontal axis path labeled as k_{\parallel} is shown by the black arrows in (b), where the beginning of the path is shown by a black point. The characteristic \mathbf{k} points are indicated by green arrows in (b), and the corresponding \mathbf{k} points are shown by the same symbols in (b). The number of k_{\parallel} mesh in (c) is 88 on the BFSs. The energy unit is taken as eV.

The pair potential term is written in the form:

$$\begin{aligned} \mathcal{H}_{\Delta} = & \sum_{\mathbf{k}} \sum_{\sigma\sigma'} [(\delta\sigma^x + i\Delta_0\sigma^y)i\sigma^y]_{\sigma\sigma'} \\ & \times \left(\sum'_{\lambda < \lambda'} c_{k\lambda\sigma}^\dagger c_{-k\lambda'\sigma'}^\dagger - \sum'_{\lambda > \lambda'} c_{k\lambda'\sigma}^\dagger c_{-k\lambda\sigma'}^\dagger \right) + \text{H.c.} \\ & + \sum_{\mathbf{k}} \sum_{\lambda \in \text{FS}} \Delta_{\lambda}(\mathbf{k}) c_{k\lambda\uparrow}^\dagger c_{-k\lambda\downarrow}^\dagger + \text{H.c.}, \end{aligned} \quad (13)$$

where the summation of $\lambda \in \text{FS}$ is taken over $\text{FS} = \{1, 2, 3, 4\}$, which reflects the fact that the electrons constituting the Fermi surfaces participate in the Cooper-pair condensation. $\sum'_{\lambda \geq \lambda'}$ indicates that the summation is taken if at least one of the bands λ and λ' has a Fermi surface. Δ_0, δ are interband pair potentials, and $\Delta_{\lambda}(\mathbf{k})$ is an intraband pair potential. σ^x and σ^y are x and y components of the Pauli matrices, respectively. Note that the interband pairing term breaks the time-reversal symmetry, because this term has a form of $\sim\sigma^x + i\sigma^y$. Since these microscopic parameters are not explicitly known, we take the extended s -wave intraband pair potential $\Delta_{\lambda}(\mathbf{k}) = \Delta_{0\lambda} + \Delta_{1\lambda} \cos(k_x/2) \cos(k_y/2)$ ($\lambda \in \text{FS}$) for a concrete calculation and for estimation of the order of magnitude of physical quantities. Each parameter is chosen

as follows: $\delta = \Delta_0 = 0.03$, $\Delta_{0,\lambda=1} = 0.03$, $\Delta_{0,\lambda=2} = 0.07$, $\Delta_{0,\lambda=3} = 0.05$, $\Delta_{0,\lambda=4} = 0.05$, $\Delta_{1,\lambda=1} = 0.01$, $\Delta_{1,\lambda=2} = 0.01$, $\Delta_{1,\lambda=3} = -0.02$, $\Delta_{1,\lambda=4} = -0.02$. (The unit is eV.) The resulting BFSs [shown in Fig. 3(a)] resemble the one shown in Ref. [16].

We define the Nambu spinor by $\tilde{\Psi}_{\mathbf{k}} = (c_{k1\uparrow}, c_{k1\downarrow}, c_{k2\uparrow}, \dots, c_{kM\downarrow}, c_{-k1\uparrow}^\dagger, \dots, c_{-kM\downarrow}^\dagger)^\top$, with $M_b = 2 \times 2 \times M$ components (each of which corresponds to Nambu, spin, and band spaces). Then, the BdG Hamiltonian is written as

$$\begin{aligned} \mathcal{H}_0 &= \mathcal{H}_N + \mathcal{H}_\Delta \\ &= \sum_{\mathbf{k} \in \text{HBZ}} \tilde{\Psi}_{\mathbf{k}}^\dagger \check{H}_0(\mathbf{k}) \tilde{\Psi}_{\mathbf{k}}, \end{aligned} \quad (14)$$

where the summation of \mathbf{k} is taken over the half Brillouin zone (HBZ, $k_y < 0$). We introduced the matrix representation of the Hamiltonian at \mathbf{k} as $\check{H}_0(\mathbf{k}) = \tau^0 \otimes \hat{H}_N(\mathbf{k}) \otimes \sigma^0 + \check{H}_\Delta(\mathbf{k})$, where $\check{H}_\Delta(\mathbf{k})$ is the matrix form of the pair potential part defined in Eq. (13) in the Nambu basis, and τ^0, σ^0 are two-dimensional identity matrices in Nambu space and spin space, respectively. We also define the unitary transformation to the bogolon basis as

$$[\tilde{\Psi}_{\mathbf{k}}]_j = \sum_b [\check{U}(\mathbf{k})]_{jb} \tilde{\alpha}_{kb}. \quad (15)$$

where $\tilde{\alpha}_{\mathbf{k}} = (\alpha_{k1}, \dots, \alpha_{k2M}, \alpha_{-k1}^\dagger, \dots, \alpha_{-k2M}^\dagger)^\top$. $j = 1, \dots, M_b$ is an index of the spinor in the electron basis, while $b = 1, \dots, M_b$ is an index of the spinor in the bogolon basis. Then, Eq. (14) can be rewritten as

$$\mathcal{H}_0 = \sum_{\mathbf{k} \in \text{HBZ}} \tilde{\alpha}_{\mathbf{k}}^\dagger \check{\mathcal{E}}(\mathbf{k}) \tilde{\alpha}_{\mathbf{k}}, \quad (16)$$

where

$$\begin{aligned} \check{U}(\mathbf{k})^\dagger \check{H}_0(\mathbf{k}) \check{U}(\mathbf{k}) &= \check{\mathcal{E}}(\mathbf{k}) \\ &= \text{diag}(E_{k1}, \dots, E_{kM_b}). \end{aligned} \quad (17)$$

Figure 3(a) shows the BFSs (red lines) together with the normal Fermi surfaces (gray solid lines). The magnified view of the BFSs is shown in (b), and the \mathbf{k} -dependent spectra are also shown in (c). Since the BFSs are topologically protected, we have identified the Bogoliubov Fermi wave vector by the sign change of the Pfaffian $\text{Pf}(\check{H}_0(\mathbf{k}))$ for the antisymmetrized Hamiltonian [7,8,16,49]

$$\check{H}_0(\mathbf{k}) = \check{W} \check{H}_0(\mathbf{k}) \check{W}^\dagger, \quad (18)$$

where

$$\check{W} = \frac{1}{\sqrt{2}} \begin{pmatrix} 1 & 1 \\ i & -i \end{pmatrix} \otimes I \otimes \sigma^0. \quad (19)$$

I is the identity matrix with the dimension M (band space). We note that the eigenvalues E_{kb} of the Kramers pair states are not degenerate because of the time-reversal symmetry broken pair potential in Eq. (13). Therefore, there are two bands of bogolons $b = 1, 2$ crossing at the Fermi level (one is the particle band and the other is the antiparticle band), which constitute the BFSs.

C. Phase of the wave function at each \mathbf{k}

Since we consider the local impurity in this paper, we need to define the impurity potential in the Wannier function basis, as will be mentioned in Sec. IV B. On the other hand, the pair potential is defined in the band basis (λ), and then the phase of the eigenfunctions in the normal state must be determined with careful thought. Namely, although the transformation $\mathbf{v}(\mathbf{k})_\lambda \rightarrow e^{i\theta_\lambda(\mathbf{k})} \mathbf{v}(\mathbf{k})_\lambda$ (i.e., $c_{k\lambda\sigma} \rightarrow e^{i\theta_\lambda(\mathbf{k})} c_{k\lambda\sigma}$) makes the eigenenergy invariant, the spectral function with local impurity depends on the choice of the phase of the normal state wave function $\mathbf{v}(\mathbf{k})_\lambda$.

We note that the fourfold rotational symmetry can be broken when we introduce the impurity potential in the Wannier function basis. This is because we choose the phase of $\mathbf{v}(\mathbf{k})_\lambda$ without fourfold symmetry as explained below, which will affect the spectral functions [see Fig. 4(b)]. If we gave the impurity potential in the band basis, the spectral function would depend only on the superconducting state wave function $U(\mathbf{k})$, and the fourfold symmetry could be preserved. In this paper, we do not respect the fourfold symmetry, which is consistent with the absence of fourfold symmetry in the experimental results [38].

Let us now discuss a specific methodology for determining the phase. As will be discussed in Sec. V, we will concentrate on the low-energy contribution near the BFSs, and hence it is necessary to construct a smooth function for the paths along BFSs C_Γ, C_{M1}, C_{M2} [shown in Figs. 3(a) and 3(b)]. We also choose the phase so as to preserve the inversion symmetry with which the theoretical results are consistent with the experiment [38]. Since our motivation is order estimation of the impurity effect on the single-particle spectral function, we take a simple setup, and no further symmetry constraint is imposed. More specifically, we consider a (nontwisted) parallel-transport gauge for C_{M1}, C_{M2} and a twisted parallel-transport gauge with inversion symmetry for C_Γ [50]. Let us write the eigenvector with the parallel-transport gauge as $\bar{\mathbf{v}}(\mathbf{k})$ and the numerically obtained one as $\mathbf{v}_{\text{num}}(\mathbf{k})$. We fix the phase at the beginning point \mathbf{k}_0 for each path as $\bar{\mathbf{v}}(\mathbf{k}_0)_\lambda = \mathbf{v}(\mathbf{k}_0)_\lambda$ [indicated by the black dot in Fig. 3(b)]. The phase of the next \mathbf{k} -point is chosen as it is parallel to the previous point. For this purpose, we first introduce the relative phase between \mathbf{k} and $\mathbf{k} + \Delta\mathbf{k}$ as

$$\varphi_\lambda(\mathbf{k}) = -\text{Im} \ln \bar{\mathbf{v}}(\mathbf{k})_\lambda \cdot \mathbf{v}_{\text{num}}(\mathbf{k} + \Delta\mathbf{k})_\lambda. \quad (20)$$

This quantity corresponds to the Berry connection in a continuous limit. Then we define the eigenvector with a parallel-transport gauge at $\mathbf{k} + \Delta\mathbf{k}$ as

$$\bar{\mathbf{v}}(\mathbf{k} + \Delta\mathbf{k})_\lambda = e^{i\varphi_\lambda(\mathbf{k})} \mathbf{v}_{\text{num}}(\mathbf{k} + \Delta\mathbf{k})_\lambda. \quad (21)$$

In this gauge, $\bar{\mathbf{v}}(\mathbf{k})_\lambda$ and $\bar{\mathbf{v}}(\mathbf{k} + \Delta\mathbf{k})_\lambda$ become parallel:

$$-\text{Im} \ln \bar{\mathbf{v}}(\mathbf{k})_\lambda \cdot \bar{\mathbf{v}}(\mathbf{k} + \Delta\mathbf{k})_\lambda = 0. \quad (22)$$

The Berry phase ϕ_C can be calculated numerically by the summation of the left-hand side of Eq. (22) taken over the closed paths $C = C_{M1}, C_{M2}$ (defined in $k_y < 0$). We obtain $\phi_C = 0$ because of the inversion symmetry and time-reversal symmetry of the normal state. For their counterparts ($k_y > 0$), we can obtain the smooth and inversion symmetric eigenvectors by using the symmetry operation defined in Eq. (B7).

For unclosed paths C_Γ [see Fig. 3(b)], we choose the twisted parallel transport gauge $\tilde{\mathbf{v}}(\mathbf{k})$ constructed from $\bar{\mathbf{v}}(\mathbf{k})$. In numerical calculation, we calculate $\bar{\mathbf{v}}(\mathbf{k}_0)_\lambda, \dots, \bar{\mathbf{v}}(\mathbf{k}_{N_\Gamma-1})_\lambda$ on the path C_Γ , and we determine $\bar{\mathbf{v}}(-\mathbf{k}_0)_\lambda$ by using inversion symmetric operation for $\bar{\mathbf{v}}(\mathbf{k}_0)_\lambda$ [see Eq. (B7) in Appendix B]. Then, we calculate the relative phase between $\bar{\mathbf{v}}(\mathbf{k}_{N_\Gamma-1})_\lambda$ and $\bar{\mathbf{v}}(-\mathbf{k}_0)_\lambda$, which is written as

$$\varphi'_\lambda = -\text{Im} \ln \bar{\mathbf{v}}(\mathbf{k}_{N_\Gamma-1})_\lambda \cdot \bar{\mathbf{v}}(-\mathbf{k}_0)_\lambda. \quad (23)$$

Finally, we define the twisted parallel transport for the n th point ($n = 0, \dots, N_\Gamma - 1$) of the path by twisting the phase at each point

$$\tilde{\mathbf{v}}(\mathbf{k}_n)_\lambda = e^{i\varphi'_\lambda n/N_\Gamma} \bar{\mathbf{v}}(\mathbf{k}_n)_\lambda. \quad (24)$$

This choice of gauge results in a smooth and inversion-symmetry-preserved eigenvector.

IV. IMPURITY EFFECTS AND GREEN'S FUNCTIONS

In this section, we proceed to a concrete analysis of the impurity effects. We use the Green's function method, which is appropriate for the analysis of the impurity effect on the superconducting system [51,52]. We calculate the spectral function, which is an experimentally observable quantity.

A. Definition of Green's functions and self-energies

First, we define the Green's function as

$$\check{G}_k(\tau) = -\langle \mathcal{T} \check{\Psi}_k(\tau) \check{\Psi}_k^\dagger \rangle = \begin{pmatrix} G_k(\tau) & F_k(\tau) \\ F_k^\dagger(\tau) & \bar{G}_k(\tau) \end{pmatrix}, \quad (25)$$

where \mathcal{T} represents imaginary time ordering, $\langle \dots \rangle$ is a statistical average, and $A(\tau) = e^{\tau \mathcal{H}} A e^{-\tau \mathcal{H}}$ is the Heisenberg representation with imaginary time. G_k, F_k correspond to the normal and anomalous Green's functions, respectively, and their conjugate quantities are \bar{G}_k, F_k^\dagger . The Fourier transformation from imaginary time to Matsubara frequency is defined as

$$\check{G}_k(i\omega_n) = \int_0^{1/T} d\tau \check{G}_k(\tau) e^{i\omega_n \tau}, \quad (26)$$

where T is a temperature. Using the clean limit Hamiltonian $\check{H}_0(\mathbf{k})$ in Eq. (14), the self-energy is also introduced by

$$\check{G}_k(i\omega_n)^{-1} = i\omega_n \check{1} - \check{H}_0(\mathbf{k}) - \check{\Sigma}_k(i\omega_n). \quad (27)$$

potential as follows:

$$\begin{aligned} \Sigma_{k\lambda\sigma,\lambda'\sigma'}(i\omega_n) &= \frac{1}{N} \sum_{\mathbf{k}_1 \in \text{HBZ}} \sum_{\lambda_1\lambda_2\sigma_1\sigma_2} [\mathcal{U}_{\lambda\sigma,\lambda_1\sigma_1,\lambda_2\sigma_2,\lambda'\sigma'}(\mathbf{k}, \mathbf{k}_1, \mathbf{k}_1, \mathbf{k}) \\ &\quad \times G_{k_1\lambda_1\sigma_1,\lambda_2\sigma_2}(i\omega_n) - \mathcal{U}_{\lambda\sigma,\lambda_1\sigma_1,\lambda_2\sigma_2,\lambda'\sigma'}(\mathbf{k}, -\mathbf{k}_1, -\mathbf{k}_1, \mathbf{k}) \bar{G}_{k_1\lambda_2\sigma_2,\lambda_1\sigma_1}(-i\omega_n)], \end{aligned} \quad (33)$$

$$\begin{aligned} S_{k\lambda\sigma,\lambda'\sigma'}(i\omega_n) &= -\frac{1}{N} \sum_{\mathbf{k}_1 \in \text{HBZ}} \sum_{\lambda_1\lambda_2\sigma_1\sigma_2} [\mathcal{U}_{\lambda\sigma,\lambda_1\sigma_1,\lambda'\sigma',\lambda_2\sigma_2}(\mathbf{k}, \mathbf{k}_1, -\mathbf{k}, -\mathbf{k}_1) \\ &\quad \times F_{k_1\lambda_1\sigma_1,\lambda_2\sigma_2}(i\omega_n) - \mathcal{U}_{\lambda\sigma,\lambda_1\sigma_1,\lambda'\sigma',\lambda_2\sigma_2}(\mathbf{k}, -\mathbf{k}_1, -\mathbf{k}, \mathbf{k}_1) F_{k_1\lambda_2\sigma_2,\lambda_1\sigma_1}(-i\omega_n)], \end{aligned} \quad (34)$$

Each component of the self-energy is expressed as $\check{\Sigma}_k = \begin{pmatrix} \Sigma_k & S_k \\ S_k^\dagger & \bar{\Sigma}_k \end{pmatrix}$.

B. Impurity potential

We now explain the impurity potential part. It is convenient to deal with the real-space representation for the disorder potential. We start from the expression written by the field operator ψ, ψ^\dagger as follows:

$$\mathcal{H}_{\text{imp}} = \sum_i \sum_{\sigma\sigma'} \int d\mathbf{r} \psi_\sigma^\dagger(\mathbf{r}) U_{\text{imp}}^{\sigma\sigma'}(\mathbf{r} - \mathbf{r}_i) \psi_{\sigma'}(\mathbf{r}), \quad (28)$$

where $U_{\text{imp}}^{\sigma\sigma'}(\mathbf{r} - \mathbf{r}_i)$ is an impurity potential with spin σ, σ' , and \mathbf{r}_i is a scattering center. We can move to the Wannier function basis from Eq. (28) by expanding the field operator, which is written as

$$\psi_\sigma(\mathbf{r}) = \sum_{\mathbf{n}} \sum_{a\gamma} w_\gamma(\mathbf{r} - \mathbf{R}_n - \mathbf{d}_a) c_{\gamma\sigma}(\mathbf{R}_n + \mathbf{d}_a). \quad (29)$$

Inserting Eq. (29) into Eq. (28), we obtain the impurity potential part of the Hamiltonian,

$$\begin{aligned} \mathcal{H}_{\text{imp}} &= \int \frac{d\mathbf{q}}{(2\pi)^3} \sum_{\mathbf{k}, \mathbf{k}'} \sum_{\lambda, \lambda', \sigma, \sigma'} \sum_{aa'\gamma\gamma'} \rho_q U_{\text{imp}}^{\sigma\sigma'}(\mathbf{q}) \\ &\quad \times f_{a\gamma, a'\gamma'}^{kk'}(\mathbf{q}) [\hat{V}(\mathbf{k})^\dagger]_{\lambda, a\gamma} [\hat{V}(\mathbf{k}')]_{a'\gamma', \lambda'} c_{k\lambda\sigma}^\dagger c_{k'\lambda'\sigma'}, \end{aligned} \quad (30)$$

where the form factor $f_{a\gamma, a'\gamma'}^{kk'}(\mathbf{q})$ can be written as

$$\begin{aligned} f_{a\gamma, a'\gamma'}^{kk'}(\mathbf{q}) &= \frac{1}{N} \sum_{\mathbf{n}, \mathbf{m}} \int d\mathbf{r} w_\gamma^*(\mathbf{r} - \mathbf{R}_n - \mathbf{d}_a) \\ &\quad \times w_{\gamma'}(\mathbf{r} - \mathbf{R}_m - \mathbf{d}_{a'}) e^{iq\mathbf{r} - ik\mathbf{R}_n + ik'\mathbf{R}_m}, \end{aligned} \quad (31)$$

and $\rho_q = \sum_i e^{-iq\mathbf{r}_i}$ is a structure factor for the impurity configuration \mathbf{r}_i . N is the number of unit cells. Note that \mathbf{q} is defined in an infinite reciprocal space, while \mathbf{k} is defined in the Brillouin zone.

Now we apply the random average for the impurity configuration,

$$\overline{\rho_q \rho_{q'}} = V n_{\text{imp}} \delta_{q, -q'}, \quad (32)$$

where $n_{\text{imp}} = V^{-1} \sum_i 1$ (V is a system volume). We consider the second-order self-energy with respect to the impurity

where

$$\begin{aligned} \mathcal{U}_{\lambda_1\sigma_1,\lambda_2\sigma_2,\lambda_3\sigma_3,\lambda_4\sigma_4}(\mathbf{k}_1,\mathbf{k}_2,\mathbf{k}_3,\mathbf{k}_4) &= n_{\text{imp}}N \int \frac{d\mathbf{q}}{(2\pi)^3} \sum_{a_1\cdots a_4} \sum_{\gamma_1\cdots\gamma_4} U_{\text{imp}}^{\sigma_1\sigma_2}(\mathbf{q}) U_{\text{imp}}^{\sigma_3\sigma_4}(-\mathbf{q}) [\hat{V}(\mathbf{k}_1)^\dagger]_{\lambda_1,a_1\gamma_1} \\ &\times [\hat{V}(\mathbf{k}_2)]_{a_2\gamma_2,\lambda_2} [\hat{V}(\mathbf{k}_3)^\dagger]_{\lambda_3,a_3\gamma_3} [\hat{V}(\mathbf{k}_4)]_{a_4\gamma_4,\lambda_4} f_{a_1\gamma_1,a_2\gamma_2}^{\mathbf{k}_1\mathbf{k}_2}(\mathbf{q}) f_{a_3\gamma_3,a_4\gamma_4}^{\mathbf{k}_3\mathbf{k}_4}(-\mathbf{q}) \delta_{\mathbf{k}_1+\mathbf{k}_3,\mathbf{k}_2+\mathbf{k}_4}. \end{aligned} \quad (35)$$

We also obtain $\bar{\Sigma}_{\mathbf{k}\lambda\sigma,\lambda'\sigma'}(i\omega_n)$ and $S_{\mathbf{k}\lambda\sigma,\lambda'\sigma'}^\dagger(i\omega_n)$ in a similar manner to the above expressions. We note that $\delta_{\mathbf{k}_1+\mathbf{k}_3,\mathbf{k}_2+\mathbf{k}_4}$ in (35) originates from the recovered-translational symmetry after the random average. Since Eqs. (33) and (34) include \mathbf{k} and $-\mathbf{k}$ in \mathcal{U} , we need to evaluate $V(\mathbf{k})$ in the full Brillouin zone, while \mathbf{k} in the left-hand side of Eqs. (33) and (34) is defined in the half-Brillouin zone. Therefore, the phase of $V(\mathbf{k})$ is fixed in the full Brillouin zone in a manner similar to Sec. III C. If we regard G, F, \bar{G}, F^\dagger as unperturbed Green's functions, we obtain the self-energy of the Born approximation. On the other hand, if we regard them as dressed Green's functions, we obtain the self-energy of the self-consistent Born approximation.

C. Evaluation of self-energies

To evaluate the self-energies, we need to define the specific form of the impurity potential $U_{\text{imp}}(\mathbf{q})$. First, we consider the case of nonmagnetic impurity (later we will also discuss the case of magnetic impurity). The impurity potential is given by

$$U_{\text{imp}}^{\sigma\sigma'}(\mathbf{q}) = U_{\text{imp}}\delta_{\sigma\sigma'}, \quad (36)$$

which is \mathbf{q} -independent and is frequently used for an electron gas model. U_{imp} is a magnitude of the potential. Although this is not a realistic impurity potential, we can further analyze the model in a simple form and make a semiquantitative estimate of the effect of impurities.

The concrete form of the form factor in Eq. (35) is written using the Wannier functions as

$$\begin{aligned} &\int \frac{d\mathbf{q}}{(2\pi)^3} f_{a_1\gamma_1,a_2\gamma_2}^{\mathbf{k}_1\mathbf{k}_2}(\mathbf{q}) f_{a_3\gamma_3,a_4\gamma_4}^{\mathbf{k}_3\mathbf{k}_4}(-\mathbf{q}) \delta_{\mathbf{k}_1+\mathbf{k}_3,\mathbf{k}_2+\mathbf{k}_4} \\ &= \frac{1}{N^2} \sum_{n_1,\dots,n_4} \int d\mathbf{r} w_{\gamma_1}^*(\mathbf{r}-\mathbf{R}_{n_1}-\mathbf{d}_{a_1}) \\ &\times w_{\gamma_2}(\mathbf{r}-\mathbf{R}_{n_2}-\mathbf{d}_{a_2}) w_{\gamma_3}^*(\mathbf{r}-\mathbf{R}_{n_3}-\mathbf{d}_{a_3}) \\ &\times w_{\gamma_4}(\mathbf{r}-\mathbf{R}_{n_4}-\mathbf{d}_{a_4}) \\ &\times e^{-i\mathbf{k}_1\cdot\mathbf{R}_{n_1}+i\mathbf{k}_2\cdot\mathbf{R}_{n_2}-i\mathbf{k}_3\cdot\mathbf{R}_{n_3}+i\mathbf{k}_4\cdot\mathbf{R}_{n_4}} \delta_{\mathbf{k}_1+\mathbf{k}_3,\mathbf{k}_2+\mathbf{k}_4}, \end{aligned} \quad (37)$$

where we have performed \mathbf{q} integration. To proceed further, we use the two approximations. First, we observe that the above quantity is expected to become largest when the locality condition $\mathbf{R}_{n_1} = \mathbf{R}_{n_2} = \mathbf{R}_{n_3} = \mathbf{R}_{n_4}$, $a_1 = a_2 = a_3 = a_4$ is satisfied. Hence, we assume that the integration of \mathbf{r} takes finite value only if it satisfies this condition. Second, although the integral can be evaluated by using the Wannier function in principle, we replace the Wannier function $w_\gamma(\mathbf{r}-\mathbf{R}_n-\mathbf{d}_a)$ with the atomic orbital function $\phi_\gamma(\mathbf{r}-\mathbf{R}_n-\mathbf{d}_a)$ for simplicity. We write the atomic orbital function as $\phi_\gamma(\mathbf{r}) = R(r)\Theta_\gamma(\theta,\varphi)$, where $R(r)$ is a radial wave function and $\Theta(\theta,\varphi)$ is the cubic harmonics for the d -orbital, whose specific form is shown in Appendix C. Then we can evaluate the

integral with respect to θ, φ by using Eq. (C7), and obtain

$$\begin{aligned} &\mathcal{U}_{\lambda_1\sigma_1,\lambda_2\sigma_2,\lambda_3\sigma_3,\lambda_4\sigma_4}(\mathbf{k}_1,\mathbf{k}_2,\mathbf{k}_3,\mathbf{k}_4) \\ &= \Gamma \mathcal{F}_{\lambda_1\sigma_1,\lambda_2\sigma_2,\lambda_3\sigma_3,\lambda_4\sigma_4}(\mathbf{k}_1,\mathbf{k}_2,\mathbf{k}_3,\mathbf{k}_4), \end{aligned} \quad (38)$$

where

$$\Gamma = \frac{5n_{\text{imp}}U_{\text{imp}}^2}{28\pi} \int dr r^2 |R(r)|^4 \quad (39)$$

and

$$\begin{aligned} &\mathcal{F}_{\lambda_1\sigma_1,\lambda_2\sigma_2,\lambda_3\sigma_3,\lambda_4\sigma_4}(\mathbf{k}_1,\mathbf{k}_2,\mathbf{k}_3,\mathbf{k}_4) \\ &= \sum_{a_1\cdots a_4} \sum_{\gamma_1\cdots\gamma_4} [\hat{V}(\mathbf{k}_1)^\dagger]_{\lambda_1,a_1\gamma_1} [\hat{V}(\mathbf{k}_2)]_{a_2\gamma_2,\lambda_2} \\ &\times [\hat{V}(\mathbf{k}_3)^\dagger]_{\lambda_3,a_3\gamma_3} [\hat{V}(\mathbf{k}_4)]_{a_4\gamma_4,\lambda_4} \\ &\times (\delta_{\gamma_1,\gamma_2}\delta_{\gamma_3,\gamma_4} + \delta_{\gamma_1,\gamma_3}\delta_{\gamma_2,\gamma_4} + \delta_{\gamma_1,\gamma_4}\delta_{\gamma_2,\gamma_3}) \\ &\times \delta_{a_1,a_2}\delta_{a_2,a_3}\delta_{a_3,a_4}\delta_{\sigma_1\sigma_2}\delta_{\sigma_3\sigma_4}. \end{aligned} \quad (40)$$

Once this form factor is obtained, we can immediately evaluate the self-energies by using Eqs. (33) and (34).

In this paper, we consider the two types of magnetic impurity (Heisenberg type, Ising type) in addition to nonmagnetic impurity. In the case of the isotropic magnetic impurity (Heisenberg type), we replace the form factor of the spins in Eq. (40) as

$$\delta_{\sigma_1\sigma_2}\delta_{\sigma_3\sigma_4} \rightarrow \boldsymbol{\sigma}_{\sigma_1\sigma_2} \cdot \boldsymbol{\sigma}_{\sigma_3\sigma_4} = 2\delta_{\sigma_1\sigma_4}\delta_{\sigma_2\sigma_3} - \delta_{\sigma_1\sigma_2}\delta_{\sigma_3\sigma_4} \quad (41)$$

for spin $S = 1/2$. We can also consider the magnetic impurity with anisotropy in the z -direction (Ising type):

$$\delta_{\sigma_1\sigma_2}\delta_{\sigma_3\sigma_4} \rightarrow \sigma_{\sigma_1\sigma_2}^z \sigma_{\sigma_3\sigma_4}^z. \quad (42)$$

Thus, the parameters that control the impurity effect are the scattering strength Γ and the type of the impurity potential (nonmagnetic or Ising type/Heisenberg type).

In the next section, Sec. V, we will discuss the parameter Γ dependence of single-particle spectra.

V. NUMERICAL RESULTS FOR SINGLE-PARTICLE SPECTRA

In the above, we have formulated the theory of the disordered BFS. Here we explain the method of calculation for the physical quantities such as single-particle excitation spectra. We also show the numerical results in the following subsections.

A. Single-particle spectra near the Fermi level

From the Green's function, we can calculate the DOS. Using the retarded Green's function $\check{G}_k(\omega + i0^+)$ obtained by the analytic continuation from imaginary axis to real axis, we

define the DOS as

$$D(\omega) = -\frac{1}{N\pi} \text{Tr} \text{Im} \sum_{k \in \text{HBZ}} \check{G}_k(\omega + i0^+). \quad (43)$$

Similar to the Fermi liquid theory of electrons, the low-energy contributions are extracted in order to see the detailed structure near the BFSs. The concrete calculation procedure is shown in Appendix D. We write down the final result,

$$D(\omega) = D_0 \sum_C \int_C d\mathbf{k} A_k(\omega), \quad (44)$$

where

$$\begin{aligned} A_k(\omega) = & \sum_{b \in \text{BFS}} \frac{V_c}{(2\pi)^2 |v_b(\mathbf{k})| D_0} \\ & \times \text{Re} \left[\frac{\text{sgn} \text{Im} \varepsilon_{k+}(\omega + i0^+) - \text{sgn} \text{Im} \varepsilon_{k-}(\omega + i0^+)}{\varepsilon_{k+}(\omega + i0^+) - \varepsilon_{k-}(\omega + i0^+)} \right. \\ & \left. \times (2\omega - [\check{\Sigma}'_k(\omega + i0^+)]_{11} - [\check{\Sigma}'_k(\omega + i0^+)]_{22}) \right] \end{aligned} \quad (45)$$

is the wave-vector-resolved spectral function, and

$$D_0 = \sum_C \int_C d\mathbf{k} \frac{V_c}{2\pi^2 |v_b(\mathbf{k})|} \quad (46)$$

is a zero-energy DOS in the clean limit. $\int_C d\mathbf{k}$ is the path integral along the BFS, which is taken over the specific path $C = C_\Gamma, C_{M1}, C_{M2}$ [see Fig. 3(b)]. $\check{\Sigma}'_k$ is the self-energy of a bogolon defined by Eq. (D1) in Appendix D, where the prime (') symbol indicates the basis of the bogolon picture. $\varepsilon_{k\pm}$ is a quantity dependent on the self-energies defined in Appendix D. In the clean limit, it reduces to

$$A_k^0 = \frac{V_c}{\pi^2 D_0 |v_b(\mathbf{k})|} \quad (47)$$

whose values are plotted in Fig. 3(c). Since the \mathbf{k} dependence originates only from the velocity $v_b(\mathbf{k})$, A_k^0 has fourfold symmetry if the energy eigenvalue E_{kb} is fourfold symmetric in \mathbf{k} -space. A_k^0 in (c) has characteristic peaks in C_{M1} and C_{M2} (indicated by green arrows). These peaks correspond to the points where the BFS has a large curvature. In contrast, the behavior of A_k^0 in C_Γ is nearly constant, where the curve of the BFS is gentle.

Here, let us comment on the relevance to experimental observation. To compare directly with the experimental result such as the tunneling experiment, we need to calculate the DOS only for the electron component, which is expressed as $D_{\text{exp}}(\omega) = -\frac{1}{N\pi} \sum_{k \in \text{BZ}} \text{Im} \text{Tr} G_k(\omega + i0^+) = -\frac{1}{N\pi} \sum_{k \in \text{HBZ}} \text{Im} \text{Tr} [G_k(\omega + i0^+) - \check{G}_k(-\omega - i0^+)]$. On the other hand, our definition of the DOS written by Eq. (43) corresponds to the direct summation of electron and hole components. The two expressions $D(\omega)$ and $D_{\text{exp}}(\omega)$ are connected by the relation $D(\omega) + D(-\omega) = D_{\text{exp}}(\omega) + D_{\text{exp}}(-\omega)$. This relation needs to be used when comparing the results with experiments.

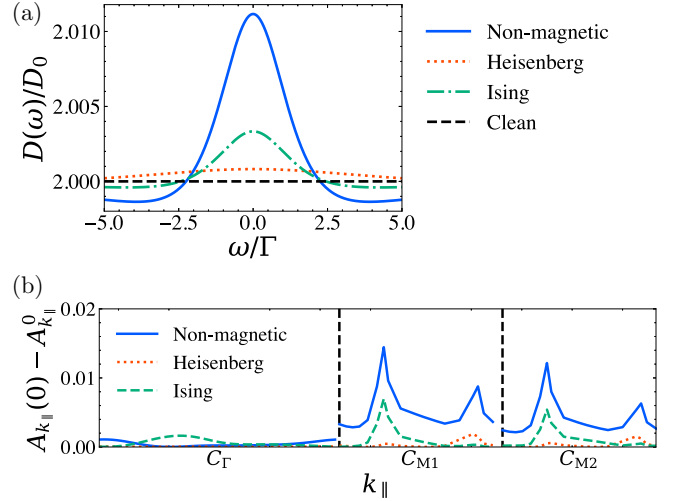


FIG. 4. Comparison between different kinds of impurities. (a) Energy dependence of the density of states, (b) wave-vector-dependent spectral function on the BFSs. The horizontal axis of (b) is taken in the same way as Fig. 3(c).

B. Born approximation

Substituting the Green's function in the clean limit to the self-energies in Eqs. (33) and (34), we obtain the self-energies in the Born approximation. We note that the self-energies do not have ω -dependence in the present setup (it appears in the self-consistent Born approximation, as shown later). Inserting the self-energies into Eq. (45), we obtain the spectral function.

Figure 4(a) shows the DOS defined in Eq. (43) (the more specific form is shown in Appendix D). Here the value is normalized by the one in the clean limit [Eq. (46)], and we consider the three kinds of impurities explained in Sec. IV C. We find the zero-energy peak in the DOS, which is absent in the clean limit. It is notable that the peak height does not depend on the impurity density and the magnitude of the impurity potential, since $\check{\Sigma}' \propto \Gamma (\propto n_{\text{imp}} U_{\text{imp}}^2)$ [see Eqs. (33), (34), (38), and (39)] and then Γ is canceled in Eq. (D7). This fact will be checked again by using the spectral function written by the bogolon basis in Eq. (50). On the other hand, the peak height changes depending on the type of impurity potential. With these results, we can roughly estimate the order of this peak height: it is about 1% of the clean-limit DOS D_0 in the case of nonmagnetic impurity.

Figure 4(b) shows the wave-vector-resolved spectral functions at each \mathbf{k} point on the BFSs. To see the effect of impurity, the difference between the spectral function with and without impurities is plotted. The differences $A_{k_{\parallel}}(0) - A_{k_{\parallel}}^0$ vary depending on the type of impurity, and the relative height varies across different regions within the Brillouin zone. The results in Fig. 4(b) are correlated with Fig. 3(c): the deviation $A_{k_{\parallel}}(0) - A_{k_{\parallel}}^0$ is large when the spectral function in the clean limit is large.

Next, we discuss the self-energies near the BFSs. Since the self-energies of the bogolon satisfy the relations $[\check{\Sigma}'_k(\omega + i0^+)]_{11} = -[\check{\Sigma}'_k(-\omega + i0^+)]_{22}^*$ and $[\check{\Sigma}'_k(\omega + i0^+)]_{12} = -[\check{\Sigma}'_k(-\omega + i0^+)]_{21}^*$ from hermiticity

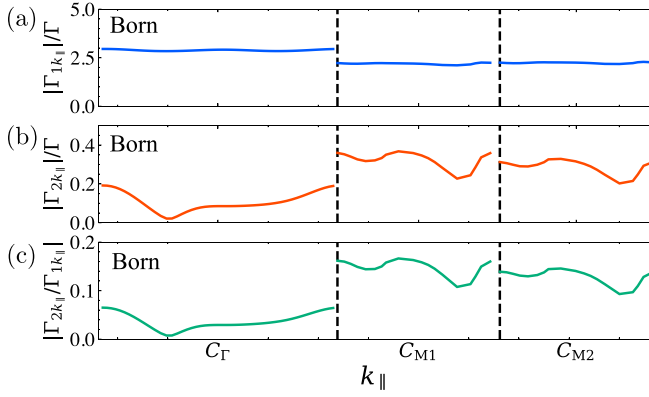


FIG. 5. Self-energies of the bogolon obtained by the Born approximation for (a) the normal part, (b) the anomalous part, and (c) the ratio of the normal and anomalous parts. The horizontal axis is taken in the same way as Fig. 3(c).

and inversion symmetry, the spectral function in Eq. (45) is determined by the following two quantities:

$$-i\Gamma_{1k}(\omega) = [\tilde{\Sigma}'_k(\omega + i0^+)]_{11}, \quad (48)$$

$$-i\Gamma_{2k}(\omega) = [\tilde{\Sigma}'_k(\omega + i0^+)]_{12}. \quad (49)$$

Γ_{1k} , Γ_{2k} are identical, respectively, to the normal and anomalous self-energies for bogolons at the low-energy regime as discussed in Sec. II. The zero-energy limit of the spectral function is given as follows:

$$\frac{A_k(\omega \rightarrow 0)}{A_k^0} = \frac{1}{\sqrt{1 - [|\Gamma_{2k}(\omega \rightarrow 0)|/\text{Re } \Gamma_{1k}(\omega \rightarrow 0)]^2}}, \quad (50)$$

where the spectral function is controlled by the ratio Γ_{2k}/Γ_{1k} . We note that this expression can be used for $\Gamma_{k1} > 0$. Since Γ_{1k} and Γ_{2k} are proportional to Γ , $A_k(\omega \rightarrow 0)$ does not depend on the impurity density and the magnitude of the impurity potential as mentioned above. While the \mathbf{k} dependence is neglected in Ref. [25] for simplicity, this paper takes full account of it on the BFSs.

Figure 5 shows the wave-vector-dependent self-energies of the bogolon for the Born approximation, where the ω -dependence is absent. Figures 5(a), 5(b) and 5(c) correspond to the normal part $|\Gamma_{1k}|$, the anomalous part $|\Gamma_{2k}|$, and their ratio $|\Gamma_{2k}/\Gamma_{1k}|$, respectively. The anomalous part $|\Gamma_{2k}|$ has a stronger $k_{||}$ -dependence in comparison to the normal part $|\Gamma_{1k}|$. Then the $k_{||}$ -dependence of $|\Gamma_{2k}/\Gamma_{1k}|$, which determines the height of the spectral function according to Eq. (50), resembles that of $|\Gamma_{2k}|$. The absolute values can be roughly estimated as $|\Gamma_{1k}|/\Gamma \sim 1$, $|\Gamma_{2k}|/\Gamma \sim 0.1$, and then $|\Gamma_{2k}/\Gamma_{1k}| \sim 0.1$. Since the square of $|\Gamma_{2k}/\Gamma_{1k}|$ (~ 0.01) determines the spectral functions, the peak value in the DOS becomes 0.5% of that in the clean limit, as shown in Fig. 4(a).

Although the detection of such a small change in the DOS might be difficult experimentally, our result indicates that, upon systematically increasing the impurity scattering, the DOS peak height remains unchanged while the peak width increases. This behavior originates from the impurity effect characteristic for BFSs, where the odd-frequency pair poten-

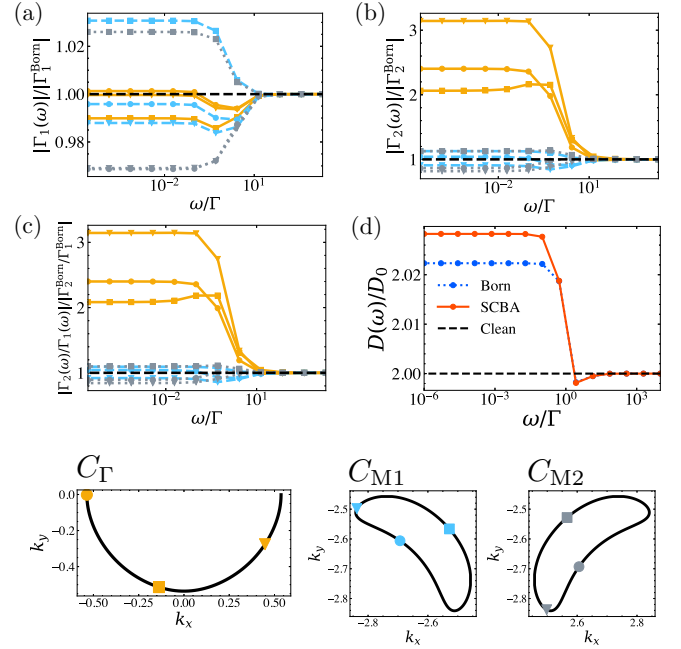


FIG. 6. (a)–(c) ω -dependence of self-energies for bogolons obtained by the self-consistent Born approximation, which is normalized by the value for the Born approximation. The colors and symbols of each line correspond to those of C_{Γ} , C_{M1} , C_{M2} shown in the bottom of the figure. (d) Density of states. The number of $k_{||}$ mesh is 18 on the BFSs.

tial (Γ_{2k}) is involved. We note that these results are obtained based on an effective theory with low-energy degrees of freedom near BFSs in the presence of a weak impurity scattering. Although the pair breaking effect from the interaction may also be expected, this effect will vanish in the low-frequency limit within the Bogoliubov Fermi liquid theory [25].

We also comment on the relation to our previous work [25], in which we studied the impurity effect on BFSs by using a simplified low-energy effective model of a bogolon. We have neglected the \mathbf{k} -dependence of Γ_{1k} and Γ_{2k} for simplicity and observed a peak structure in the DOS. This behavior is qualitatively consistent with the results of the DOS in the present paper. Here we have further clarified the $k_{||}$ -dependence of the self-energies and estimated the order of magnitude of spectra.

C. Self-consistent Born approximation

Next, we consider the self-consistent Born approximation. We obtain the self-energies by solving Eqs. (33) and (34) self-consistently. The concrete forms of the Green's functions are shown in Appendix D.

Figures 6(a)–6(c) show the ω -dependence of the self-energies of a bogolon, which are normalized by the value for the Born approximation. We have chosen several \mathbf{k} points on the BFSs C_{Γ} , C_{M1} , C_{M2} shown in the bottom part of Fig. 6. We confirm that each quantity coincides with that of the Born approximation at large ω , as expected. On the other hand, these quantities change at small frequencies because of the mixing of normal and anomalous parts by the self-consistent calculation. $|\Gamma_{1k}(\omega)|$ is not much changed from

the Born approximation as seen from Fig. 6(a). On the contrary, $|\Gamma_{2k}(\omega)|$ becomes larger at low frequency for C_Γ . Hence $|\Gamma_{2k}(\omega)/\Gamma_{1k}(\omega)|$ becomes larger. This behavior results in the larger peak height of the DOS as shown in Fig. 6(d) compared to the Born approximation. This is because the peak height is determined by $\Gamma_{2k}(\omega \rightarrow 0)/\Gamma_{1k}(\omega \rightarrow 0)$ as discussed in the previous subsection.

We comment on a spectrum in the experimental setup. The observed DOS has a finite resolution $\Delta\omega$, which is determined by the detailed experimental condition. Then, the expected behavior of the observed DOS becomes $D_{\text{observed}} = \frac{1}{\Delta\omega} \int_{-\Delta\omega/2}^{\Delta\omega/2} d\omega D(\omega)$, which smoothly goes to the clean limit if $\Gamma \ll \Delta\omega$. We expect the presence of a zero-energy peak when $\Gamma \gg \Delta\omega$, whereas in the opposite case $\Gamma \ll \Delta\omega$, the peak will be masked.

Finally, we mention the two kinds of solutions in the self-consistent Born approximation as proposed in Ref. [25]. In our former study, we applied the self-consistent Born approximation for an effective low-energy model for bogolons, where the \mathbf{k} dependence in self-energies is neglected. With this simplified setup, we have scanned the parameter space and found two kinds of solutions: one is a Born-approximation-like solution with $\Gamma_{1,2}(\omega) \sim \text{const}$ (first-kind), and the other is characterized by $\Gamma_{1,2}(\omega) \propto 1/\omega$ (second-kind) at low ω [25]. In the present analysis, we obtain the solution of the first-kind as shown in Figs. 6(a)–6(c), while the solution of the second-kind is not realized at least in our analysis based on iron-based superconductors.

VI. SUMMARY AND DISCUSSION

In this paper, we have analyzed the impurity effect on the Bogoliubov Fermi surface using a realistic model for iron-based materials combined with the Born approximation. We have investigated the detailed structure for the single-particle spectra at low energies. Based on the tight-binding parameters obtained from first-principles calculations, we have calculated the wave-vector-dependent dynamical self-energy focusing on the low-energy regime near the Bogoliubov Fermi surfaces. To evaluate the self-energies, we assume weak impurity scattering, which allows us to employ a conventional Born approximation as in usual metals, while the large scattering center may create an impurity bound state.

We have found that the zero-energy peak appears in the density of states as induced by the off-diagonal self-energy for bogolons. Furthermore, we have estimated an order of magnitude of the peak. The peak height is about 0.5% of the density of states in the clean limit and is independent of the impurity density and the magnitude of the potential in the Born approximation. On the other hand, the peak height varies with the type of nonmagnetic or magnetic impurities.

These features are unique to the Bogoliubov Fermi surface. Hence, a systematic study of impurity effects may provide experimental confirmation of the presence of the Bogoliubov Fermi surface in Fe(Se, S). Although we have assumed a specific pair potential in this paper, the present method can be applied to other superconducting states.

ACKNOWLEDGMENTS

This work was supported by KAKENHI Grants No. 19H01842, No. 19H05825, No. 21K03459, and No. 23KJ0298.

APPENDIX A: DETAILS OF THE FIRST-PRINCIPLES CALCULATIONS

We performed the first-principles calculations of FeSe using QUANTUM ESPRESSO (QE) [53] and constructed the tight-binding Hamiltonian with WANNIER90 [54]. In QE calculations, we used the exchange-correlation functional proposed by Perdew, Burke, and Ernzerhof [55], and the ultrasoft pseudopotentials [56] provided in PSLIBRARY [57]. The plane-wave cutoff energy and charge-density cutoff values were set to be 46 and 240 Ry, respectively. The crystal structure parameters of FeSe were obtained from experimental data [58]. However, two Fe sites were placed at (0,0,0) and (0.5,0.5,0) to increase the accuracy of the calculation in WANNIER90. Then, we constructed maximally localized Wannier functions for ten orbitals of Fe(3d). However, as is well known, the obtained band structure deviates significantly from experimental observations. Here, we have adjusted the band structure by referring to Ref. [48]; the xz/yz and $x^2 - y^2$ site energies of the two Fe sites in the unit cell were added by +0.1 and +0.04 eV, respectively. The (1,0,0) and corresponding hopping integrals of the xz/yz and $x^2 - y^2$ orbitals were added by -0.009 and -0.018 eV, respectively. The Fe(I)-Fe(II) nearest-neighbor hopping integrals for the xz/yz and $x^2 - y^2$ orbitals were added by -0.05 eV.

APPENDIX B: SYMMETRY OPERATION

We perform a symmetry operation for an annihilation operator

$$c_{\gamma\sigma}(\mathbf{R}_n + \mathbf{d}_a) \rightarrow \sum_{\gamma_1} (e^{i\theta \cdot \mathbf{L}})_{\gamma\gamma_1} c_{\gamma_1\sigma}[\alpha(\mathbf{R}_n + \mathbf{d}_a) + \mathbf{b}], \quad (\text{B1})$$

where α is an orthogonal matrix (for inversion, mirror, rotation, and these combinations) with the rotation vector θ , \mathbf{L} is an angular momentum for the d -orbital, and \mathbf{b} is a translation vector. We perform this symmetry operation to Eq. (9), and then we obtain

$$\begin{aligned} & \sum_{nm\gamma\gamma'\sigma a a'} H_{N\gamma\gamma'}(\mathbf{R}_n + \mathbf{d}_{a'} - \mathbf{d}_a) \sum_{\gamma_1\gamma_2} c_{\gamma_1\sigma}^\dagger[\alpha(\mathbf{R}_n + \mathbf{d}_a) + \mathbf{b}](e^{i\theta \cdot \mathbf{L}})_{\gamma_1\gamma'}(e^{-i\theta \cdot \mathbf{L}})_{\gamma'\gamma_2} c_{\gamma_2\sigma}[\alpha(\mathbf{R}_n + \mathbf{R}_m + \mathbf{d}_{a'}) + \mathbf{b}] \\ &= \sum_{nm\gamma\gamma'\sigma a a'} \sum_{\gamma_1\gamma_2} (e^{i\theta \cdot \mathbf{L}})_{\gamma_1\gamma'} H_{N\gamma\gamma'}[\alpha^{-1}(\mathbf{R}_n + \mathbf{d}_{a'} - \mathbf{b}) - \alpha^{-1}(\mathbf{d}_a - \mathbf{b})](e^{-i\theta \cdot \mathbf{L}})_{\gamma'\gamma_2} c_{\gamma_1\sigma}^\dagger(\mathbf{R}_n + \mathbf{d}_a) c_{\gamma_2\sigma}(\mathbf{R}_n + \mathbf{R}_m + \mathbf{d}_{a'}). \end{aligned} \quad (\text{B2})$$

After the symmetry operation $\alpha^{-1}(\mathbf{R}_n + \mathbf{d}_{a'} - \mathbf{b})$, we can define a new lattice vector $\mathbf{R}_{\tilde{n}'}$ and position of sublattice $\mathbf{d}_{\tilde{a}'}$, i.e., $\alpha^{-1}(\mathbf{R}_n + \mathbf{d}_{a'} - \mathbf{b}) = \mathbf{R}_{\tilde{n}'} + \mathbf{d}_{\tilde{a}'}$. Similarly, we write $\alpha^{-1}(\mathbf{d}_a - \mathbf{b}) = \mathbf{R}_{\tilde{n}} + \mathbf{d}_{\tilde{a}}$. Then we obtain

$$\begin{aligned} \text{Eq. (B2)} &= \sum_{nm\gamma\gamma'\sigma a a'} \sum_{\gamma_1\gamma_2} (e^{-i\theta \cdot L})_{\gamma_1\gamma_2} H_{N\gamma\gamma'}(\mathbf{R}_{\tilde{n}'} - \mathbf{R}_{\tilde{n}} + \mathbf{d}_{\tilde{a}'} - \mathbf{d}_{\tilde{a}}) \\ &\times (e^{i\theta \cdot L})_{\gamma'\gamma_2} c_{\gamma_1\sigma}^\dagger(\mathbf{R}_n + \mathbf{d}_a) c_{\gamma_2\sigma}(\mathbf{R}_n + \mathbf{R}_m + \mathbf{d}_{a'}). \end{aligned} \quad (\text{B3})$$

We can conclude that $H_{N\gamma\gamma'}(\mathbf{R}_n + \mathbf{d}_{a'} - \mathbf{d}_a)$ needs to have the symmetry

$$\begin{aligned} H_{N\gamma\gamma'}(\mathbf{R}_n + \mathbf{d}_{a'} - \mathbf{d}_a) \\ = \sum_{\gamma_1\gamma_2} (e^{-i\theta \cdot L})_{\gamma_1\gamma_2} H_{N\gamma_1\gamma_2}(\mathbf{R}_{\tilde{n}'} - \mathbf{R}_{\tilde{n}} + \mathbf{d}_{\tilde{a}'} - \mathbf{d}_{\tilde{a}}) (e^{i\theta \cdot L})_{\gamma_2\gamma_1}. \end{aligned} \quad (\text{B4})$$

Next, we consider the symmetry operation for the eigenvector $\hat{V}(\mathbf{k})$. Using $\hat{V}(\mathbf{k})$, we perform the unitary transformation from the Wannier basis to the band basis,

$$c_{ka\gamma\sigma} = \sum_{\lambda} [\hat{V}(\mathbf{k})]_{a\gamma,\lambda} c_{k\lambda\sigma}. \quad (\text{B5})$$

Since the annihilation operator is transformed as Eq. (B1), we can write

$$\begin{aligned} c_{k\lambda\sigma}^\dagger &= \frac{1}{\sqrt{N}} \sum_{a\gamma} c_{\gamma\sigma}^\dagger(\mathbf{R}_n + \mathbf{d}_a) e^{i\mathbf{k} \cdot \mathbf{R}_n} [\hat{V}(\mathbf{k})]_{a\gamma,\lambda} \\ &\rightarrow \frac{1}{\sqrt{N}} \sum_{a\gamma\gamma_1\mathbf{n}} c_{\gamma_1\sigma}^\dagger[\alpha(\mathbf{R}_n + \mathbf{d}_a) + \mathbf{b}] (e^{-i\theta \cdot L})_{\gamma_1\gamma} \\ &\times e^{i\mathbf{k} \cdot \mathbf{R}_n} [\hat{V}(\mathbf{k})]_{a\gamma,\lambda} \\ &= \frac{1}{\sqrt{N}} \sum_{a\gamma\gamma_1\mathbf{n}} c_{\gamma_1\sigma}^\dagger(\mathbf{R}_{\tilde{n}} + \mathbf{d}_{\tilde{a}}) e^{i(\alpha\mathbf{k}) \cdot \mathbf{R}_{\tilde{n}}} (e^{-i\theta \cdot L})_{\gamma_1\gamma} \\ &\times e^{i\mathbf{k} \cdot [\alpha^{-1}(\mathbf{d}_a - \mathbf{b}) - \mathbf{d}_a]} [\hat{V}(\mathbf{k})]_{\tilde{a}^{-1}\gamma,\lambda}, \end{aligned} \quad (\text{B6})$$

where $\mathbf{R}_{\tilde{n}} + \mathbf{d}_{\tilde{a}} = \alpha(\mathbf{R}_n + \mathbf{d}_a) + \mathbf{b}$ and $\alpha^{-1}(\mathbf{d}_a - \mathbf{b}) = \mathbf{R}_{\tilde{n}^{-1}} + \mathbf{d}_{\tilde{a}^{-1}}$. Then we can obtain the eigenvector at $\alpha\mathbf{k}$,

$$[\hat{V}(\alpha\mathbf{k})]_{\tilde{a}\gamma,\lambda} = \sum_{\gamma_1} (e^{-i\theta \cdot L})_{\gamma_1\gamma} e^{i\mathbf{k} \cdot [\alpha^{-1}(\mathbf{d}_a - \mathbf{b}) - \mathbf{d}_a]} [\hat{V}(\mathbf{k})]_{\tilde{a}^{-1}\gamma_1,\lambda}. \quad (\text{B7})$$

APPENDIX C: CUBIC HARMONICS

We list the cubic harmonics for d -orbital as follows:

$$\Theta_{z^2}(\theta, \varphi) = \sqrt{\frac{5}{16\pi}} (3 \cos^2 \theta - 1), \quad (\text{C1})$$

$$\Theta_{xz}(\theta, \varphi) = \sqrt{\frac{15}{4\pi}} \sin \theta \cos \theta \cos \varphi, \quad (\text{C2})$$

$$\Theta_{yz}(\theta, \varphi) = \sqrt{\frac{15}{4\pi}} \sin \theta \cos \theta \sin \varphi, \quad (\text{C3})$$

$$\Theta_{x^2-y^2}(\theta, \varphi) = \sqrt{\frac{15}{16\pi}} \sin^2 \theta \cos 2\varphi, \quad (\text{C4})$$

$$\Theta_{xy}(\theta, \varphi) = \sqrt{\frac{15}{16\pi}} \sin^2 \theta \sin 2\varphi. \quad (\text{C5})$$

These functions satisfy the orthogonal relation as

$$\int d\theta d\varphi \sin \theta \Theta_m(\theta, \varphi) \Theta_{m'}(\theta, \varphi) = \pi^2 \delta_{mm'}. \quad (\text{C6})$$

Furthermore, we can evaluate the following integral:

$$\begin{aligned} \int d\theta d\varphi \sin \theta \Theta_{\gamma_1}(\theta, \varphi) \Theta_{\gamma_2}(\theta, \varphi) \Theta_{\gamma_3}(\theta, \varphi) \Theta_{\gamma_4}(\theta, \varphi) \\ = \frac{5}{28\pi} (\delta_{\gamma_1, \gamma_2} \delta_{\gamma_3, \gamma_4} + \delta_{\gamma_1, \gamma_3} \delta_{\gamma_2, \gamma_4} + \delta_{\gamma_1, \gamma_4} \delta_{\gamma_2, \gamma_3}). \end{aligned} \quad (\text{C7})$$

In this basis, angular momentum is given by

$$L_x = \begin{pmatrix} 0 & 0 & \sqrt{3}i & 0 & 0 \\ 0 & 0 & 0 & 0 & i \\ -\sqrt{3}i & 0 & 0 & -i & 0 \\ 0 & 0 & i & 0 & 0 \\ 0 & -i & 0 & 0 & 0 \end{pmatrix}, \quad (\text{C8})$$

$$L_y = \begin{pmatrix} 0 & -\sqrt{3}i & 0 & 0 & 0 \\ \sqrt{3}i & 0 & 0 & -i & 0 \\ 0 & 0 & 0 & 0 & -i \\ 0 & i & 0 & 0 & 0 \\ 0 & 0 & i & 0 & 0 \end{pmatrix}, \quad (\text{C9})$$

$$L_z = \begin{pmatrix} 0 & 0 & 0 & 0 & 0 \\ 0 & 0 & -i & 0 & 0 \\ 0 & i & 0 & 0 & 0 \\ 0 & 0 & 0 & 0 & -2i \\ 0 & 0 & 0 & 2i & 0 \end{pmatrix}. \quad (\text{C10})$$

APPENDIX D: CALCULATION OF SINGLE-PARTICLE SPECTRA

1. Density of states

We perform the summation of \mathbf{k} in Eq. (43) focusing on the low energy. It is convenient to introduce the short-hand notation for the self-energy of a bogolon as

$$\check{\Sigma}'_k(i\omega_n) = \check{U}(\mathbf{k})^\dagger \check{\Sigma}_k(i\omega_n) \check{U}(\mathbf{k}). \quad (\text{D1})$$

Using this, the Green's function is written as follows:

$$\check{G}_k(i\omega_n) = \check{U}(\mathbf{k}) \left[i\omega_n \check{1} - \check{\mathcal{E}}(\mathbf{k}) - \check{\Sigma}'_k(i\omega_n) \right]^{-1} \check{U}(\mathbf{k})^\dagger. \quad (\text{D2})$$

Since the contribution near the BFSs becomes larger, we extract two low-energy bands of bogolon $b \in \text{BFS} = 1, 2$ which make the BFSs. For the calculation of the DOS, we change the coordinate of \mathbf{k} as $(k_x, k_y) \rightarrow (k_{\parallel}, k_{\perp})$, where k_{\parallel} is a parallel component to the BFSs and k_{\perp} is its perpendicular component. Then the integral around the path C can be rewritten by using the energy of the bogolon $\varepsilon (= E_b)$ as $dk_{\beta\parallel} dk_{\beta\perp} = dk_{\beta\parallel} d\varepsilon / |v_b(k_{\beta\parallel})|$ with Fermi velocity of the bogolon $v_b(k_{\beta\parallel})$. A similar method is used in Ref. [20]. There are three paths of the BFSs, $C = C_{\Gamma}, C_{M1}, C_{M2}$ [see Figs. 3(a) and 3(b)], in the half-Brillouin zone.

With these preliminaries, we finally obtain

$$D(\omega) = -\frac{1}{\pi} \text{Im} \sum_C \int_C d\mathbf{k} \frac{V_c}{2\pi^2 |v_b(\mathbf{k})|} \sum_{b' \in \text{BFS}} \int_{-\omega_c}^{\omega_c} d\varepsilon [(\omega + i0^+) \check{1} - \check{\mathcal{E}}(\mathbf{k}) - \check{\Sigma}'_k(\omega + i0^+)]_{b'b'}^{-1}, \quad (\text{D3})$$

where ω_c is a cutoff energy and $V_c = V/N$. $\int_C d\mathbf{k}$ is the integral of the k_{\parallel} direction, which is taken over the path C . Below we evaluate a summation of b' in Eq. (D3). The 2×2 matrix, which is enclosed in $[\dots]$, is expressed as

$$[(\omega + i0^+) \check{1} - \check{\mathcal{E}}(\mathbf{k}) - \check{\Sigma}'_k(\omega + i0^+)]_{b'b'}^{-1} = -\frac{1}{[\varepsilon - \varepsilon_{k+}(\omega + i0^+)] [\varepsilon - \varepsilon_{k-}(\omega + i0^+)]} \times \begin{pmatrix} \omega + i0^+ + \varepsilon - [\check{\Sigma}'_k(\omega + i0^+)]_{22} & [\check{\Sigma}'_k(\omega + i0^+)]_{12} \\ [\check{\Sigma}'_k(\omega + i0^+)]_{21} & \omega + i0^+ - \varepsilon - [\check{\Sigma}'_k(\omega + i0^+)]_{11} \end{pmatrix}_{bb'}, \quad (\text{D4})$$

where we use $\varepsilon_1 = -\varepsilon_2 \equiv \varepsilon$ for the inversion symmetry, and $\varepsilon_{k\pm}$ is defined as

$$\varepsilon_{k\pm}(z) = \frac{1}{2} (-[\check{\Sigma}'_k(z)]_{11} + [\check{\Sigma}'_k(z)]_{22}) \pm \frac{1}{2} ([[\check{\Sigma}'_k(z)]_{11} - [\check{\Sigma}'_k(z)]_{22}]^2 + 4((z - [\check{\Sigma}'_k(z)]_{11})(z - [\check{\Sigma}'_k(z)]_{22}) - [\check{\Sigma}'_k(z)]_{12}[\check{\Sigma}'_k(z)]_{21}))^{1/2}. \quad (\text{D5})$$

Performing the integration of ε in Eq. (D3), we obtain

$$D(\omega) = D_0 \sum_C \int_C d\mathbf{k} \frac{V_c}{2\pi^2 |v_b(\mathbf{k})| D_0} \text{Re} \left[\frac{\text{sgn Im } \varepsilon_{k+}(\omega + i0^+) - \text{sgn Im } \varepsilon_{k-}(\omega + i0^+)}{\varepsilon_{k+}(\omega + i0^+) - \varepsilon_{k-}(\omega + i0^+)} \times \left\{ 2\omega - [\check{\Sigma}'_k(\omega + i0^+)]_{b_1 b_1} - [\check{\Sigma}'_k(\omega + i0^+)]_{b_2 b_2} \right\} \right]. \quad (\text{D6})$$

2. Self-energies

We proceed to an evaluation of the self-energies. We deal with the \mathbf{k} summation in a similar manner to Eq. (D6). Then we rewrite the self-energy Eq. (33) as

$$\begin{aligned} \Sigma_{k\lambda\sigma, \lambda'\sigma'}(\omega + i0^+) &\simeq \Gamma D_0 \sum_C \int_C d\mathbf{k}_1 \frac{V_c}{2\pi^2 |v_b(\mathbf{k}_1)| D_0} \left(\mathcal{F}_{\lambda\sigma, \lambda_1\sigma_1, \lambda_2\sigma_2, \lambda'\sigma'}(\mathbf{k}, \mathbf{k}_1, \mathbf{k}_1, \mathbf{k}) \sum_{b', b''} [\check{U}(\mathbf{k}_1)]_{\lambda\sigma, b'} [\check{U}(\mathbf{k}_1)^\dagger]_{b'', \lambda'\sigma'} \right. \\ &\times \int_{-\omega_c}^{\omega_c} d\varepsilon [(\omega + i0^+) \check{1} - \check{\mathcal{E}}(\mathbf{k}_1) - \check{\Sigma}'_{\mathbf{k}_1}(\omega + i0^+)]_{b'b''}^{-1} - \mathcal{F}_{\lambda\sigma, \lambda_1\sigma_1, \lambda_2\sigma_2, \lambda'\sigma'}(\mathbf{k}, -\mathbf{k}_1, -\mathbf{k}_1, \mathbf{k}) \\ &\times \sum_{b', b''} [\check{U}(\mathbf{k}_1)]_{\lambda\sigma + M, b'} [\check{U}(\mathbf{k}_1)^\dagger]_{b'', \lambda'\sigma' + M} \int_{-\omega_c}^{\omega_c} d\varepsilon [(-\omega - i0^+) \check{1} - \check{\mathcal{E}}(\mathbf{k}_1) - \check{\Sigma}'_{\mathbf{k}_1}(-\omega - i0^+)]_{b'b''}^{-1} \Big). \quad (\text{D7}) \end{aligned}$$

We extract the contribution near the BFSs in a similar manner to Eq. (D4). Then, we obtain

$$\begin{aligned} \Sigma_{k\lambda\sigma, \lambda'\sigma'}(\omega + i0^+) &= -i\pi\Gamma \sum_{\lambda_1\lambda_2\sigma_1\sigma_2} \sum_C \int_C d\mathbf{k}_1 \frac{V_c}{2\pi^2 |v_b(k_{1\parallel})| D_0} \\ &\times \left(\mathcal{F}_{\lambda\sigma, \lambda_1\sigma_1, \lambda_2\sigma_2, \lambda'\sigma'}(\mathbf{k}, \mathbf{k}_1, \mathbf{k}_1, \mathbf{k}) \sum_{b', b''} [\check{U}(\mathbf{k}_1)]_{\lambda_1\sigma_1, b'} [G_{\mathbf{k}_1}^{\text{bog}}(\omega + i0^+)]_{b'b''} [\check{U}(\mathbf{k}_1)^\dagger]_{b'', \lambda_2\sigma_2} \right. \\ &\left. - \mathcal{F}_{\lambda\sigma, \lambda_1\sigma_1, \lambda_2\sigma_2, \lambda'\sigma'}(\mathbf{k}, -\mathbf{k}_1, -\mathbf{k}_1, \mathbf{k}) \sum_{b', b''} [\check{U}(\mathbf{k}_1)]_{\lambda_2\sigma_2 + M, b'} [G_{\mathbf{k}_1}^{\text{bog}}(-\omega - i0^+)]_{b'b''} [\check{U}(\mathbf{k}_1)^\dagger]_{b'', \lambda_1\sigma_1 + M} \right), \quad (\text{D8}) \end{aligned}$$

where

$$G_{\mathbf{k}}^{\text{bog}}(z) = \text{sgn Im } \varepsilon_{k-}(z) \sigma^z + \frac{\text{sgn Im } \varepsilon_{k+}(z) - \text{sgn Im } \varepsilon_{k-}(z)}{\varepsilon_{k+}(z) - \varepsilon_{k-}(z)} \begin{pmatrix} z - [\check{\Sigma}'_k(z)]_{22} + \varepsilon_{k+}(z) & [\check{\Sigma}'_k(z)]_{12} \\ [\check{\Sigma}'_k(z)]_{21} & z - [\check{\Sigma}'_k(z)]_{11} - \varepsilon_{k+}(z) \end{pmatrix}. \quad (\text{D9})$$

Solving Eq. (D8) on the BFSs, we can determine $\Sigma_{k\lambda\sigma, \lambda'\sigma'}(\omega + i0^+)$ self-consistently. We also calculate $S_k, \bar{S}_k, S_k^\dagger$ in a similar manner. Inserting these self-energies into Eq. (45), we obtain the spectral function $A_k(\omega)$.

- [1] For a review, see M. Sigrist and K. Ueda, *Rev. Mod. Phys.* **63**, 239 (1991).
- [2] G. E. Volovik, *JETP Lett.* **49**, 790 (1989).
- [3] G. E. Volovik, *Phys. Lett. A* **142**, 282 (1989).
- [4] W. V. Liu and F. Wilczek, *Phys. Rev. Lett.* **90**, 047002 (2003).
- [5] E. Gubankova, E. G. Mishchenko, and F. Wilczek, *Phys. Rev. Lett.* **94**, 110402 (2005); *Phys. Rev. B* **74**, 184516 (2006).
- [6] S. Autti, J. T. Mäkinen, J. Rysti, G. E. Volovik, V. V. Zavjalov, and V. B. Eltsov, *Phys. Rev. Res.* **2**, 033013 (2020).
- [7] D. F. Agterberg, P. M. R. Brydon, and C. Timm, *Phys. Rev. Lett.* **118**, 127001 (2017).
- [8] P. M. R. Brydon, D. F. Agterberg, H. Menke, and C. Timm, *Phys. Rev. B* **98**, 224509 (2018).
- [9] G. E. Volovik, *JETP Lett.* **58**, 469 (1993).
- [10] N. F. Q. Yuan and L. Fu, *Phys. Rev. B* **97**, 115139 (2018).
- [11] S. Sumita, T. Nomoto, K. Shiozaki, and Y. Yanase, *Phys. Rev. B* **99**, 134513 (2019).
- [12] H. Menke, C. Timm, and P. M. R. Brydon, *Phys. Rev. B* **100**, 224505 (2019).
- [13] J. M. Link, I. Boettcher, and I. F. Herbut, *Phys. Rev. B* **101**, 184503 (2020).
- [14] J. M. Link and I. F. Herbut, *Phys. Rev. Lett.* **125**, 237004 (2020).
- [15] H. G. Suh, H. Menke, P. M. R. Brydon, C. Timm, A. Ramires, and D. F. Agterberg, *Phys. Rev. Res.* **2**, 032023(R) (2020).
- [16] C. Setty, S. Bhattacharyya, Y. Cao, A. Kreisel, and P. J. Hirschfeld, *Nat. Commun.* **11**, 523 (2020).
- [17] C. Setty, Y. Cao, A. Kreisel, S. Bhattacharyya, and P. J. Hirschfeld, *Phys. Rev. B* **102**, 064504 (2020).
- [18] C. J. Lapp, G. Börner, and C. Timm, *Phys. Rev. B* **101**, 024505 (2020).
- [19] H. Oh and E.-G. Moon, *Phys. Rev. B* **102**, 020501(R) (2020).
- [20] S.-T. Tamura, S. Iimura, and S. Hoshino, *Phys. Rev. B* **102**, 024505 (2020).
- [21] I. F. Herbut and J. M. Link, *Phys. Rev. B* **103**, 144517 (2021).
- [22] C. Timm, P. M. R. Brydon, and D. F. Agterberg, *Phys. Rev. B* **103**, 024521 (2021).
- [23] C. Timm and A. Bhattacharya, *Phys. Rev. B* **104**, 094529 (2021).
- [24] Y.-F. Jiang, H. Yao, and F. Yang, *Phys. Rev. Lett.* **127**, 187003 (2021).
- [25] T. Miki, S.-T. Tamura, S. Iimura, and S. Hoshino, *Phys. Rev. B* **104**, 094518 (2021).
- [26] S. Hoshino and T. Miki, *J. Phys.: Conf. Ser.* **2323**, 012002 (2022).
- [27] P. Dutta, F. Parhizgar, and A. M. Black-Schaffer, *Phys. Rev. Res.* **3**, 033255 (2021).
- [28] D. Kim, S. Kobayashi, and Y. Asano, *J. Phys. Soc. Jpn.* **90**, 104708 (2021).
- [29] S. Kobayashi, A. Bhattacharya, C. Timm, and P. M. R. Brydon, *Phys. Rev. B* **105**, 134507 (2022).
- [30] T. Kitamura, S. Kanasugi, M. Chazono, and Y. Yanase, *Phys. Rev. B* **107**, 214513 (2023).
- [31] E. A. Schuberth, B. Strickler, and K. Andres, *Phys. Rev. Lett.* **68**, 117 (1992).
- [32] R. J. Zieve, R. Duke, and J. L. Smith, *Phys. Rev. B* **69**, 144503 (2004).
- [33] S. Kittaka, S. Nakamura, T. Sakakibara, N. Kikugawa, T. Terashima, S. Uji, D. A. Sokolov, A. P. Mackenzie, K. Irie, Y. Tsutsumi, K. Suzuki, and K. Machida, *J. Phys. Soc. Jpn.* **87**, 093703 (2018).
- [34] For a review, see T. Shibauchi, T. Hanaguri, and Y. Matsuda, *J. Phys. Soc. Jpn.* **89**, 102002 (2020).
- [35] T. Hanaguri, K. Iwaya, Y. Kohsaka, T. Machida, T. Watashige, S. Kasahara, T. Shibauchi, and Y. Matsuda, *Sci. Adv.* **4**, eaar6419 (2018).
- [36] Y. Sato, S. Kasahara, T. Taniguchi, X. Xing, Y. Kasahara, Y. Tokiwa, Y. Yamakawa, H. Kontani, T. Shibauchi, and Y. Matsuda, *Proc. Natl. Acad. Sci. (USA)* **115**, 1227 (2018).
- [37] Y. Mizukami, M. Haze, O. Tanaka, K. Matsuura, D. Sano, J. Böker, I. Eremin, S. Kasahara, Y. Matsuda, and T. Shibauchi, *Commun. Phys.* **6**, 183 (2023).
- [38] T. Nagashima, T. Hashimoto, S. Najafzadeh, S.-i. Ouchi, T. Suzuki, A. Fukushima, S. Kasahara, K. Matsuura, M. Qiu, Y. Mizukami, K. Hashimoto, Y. Matsuda, T. Shibauchi, S. Shin, and K. Okazaki (2022), doi:10.21203/rs.3.rs-2224728/v1.
- [39] V. L. Berezinskii, *JETP Lett.* **20**, 287 (1974).
- [40] T. R. Kirkpatrick and D. Belitz, *Phys. Rev. Lett.* **66**, 1533 (1991).
- [41] A. Balatsky and E. Abrahams, *Phys. Rev. B* **45**, 13125(R) (1992).
- [42] V. J. Emery and S. Kivelson, *Phys. Rev. B* **46**, 10812 (1992).
- [43] P. Coleman, E. Miranda, and A. Tsvelik, *Phys. Rev. Lett.* **70**, 2960 (1993).
- [44] For a review, see Y. Tanaka, M. Sato, and N. Nagaosa, *J. Phys. Soc. Jpn.* **81**, 011013 (2012).
- [45] For a review, see J. Linder and A. V. Balatsky, *Rev. Mod. Phys.* **91**, 045005 (2019).
- [46] For a review, see J. Cayao, C. Triola, and A. M. Black-Schaffer, *Eur. Phys. J.: Spec. Top.* **229**, 545 (2020).
- [47] For a review, see C. Triola, J. Cayao, and A. M. Black-Schaffer, *Ann. Phys.* **532**, 1900298 (2020).
- [48] Y. Yamakawa, S. Onari, and H. Kontani, *Phys. Rev. X* **6**, 021032 (2016).
- [49] M. Wimmer, *ACM Trans. Math. Softw.* **38**, 1 (2012).
- [50] D. Vanderbilt, *Berry Phase in Electronic Structure Theory* (Cambridge University Press, Cambridge, 2018).
- [51] A. A. Abrikosov and L. P. Gor'kov, *JETP* **8**, 1090 (1959).
- [52] A. A. Abrikosov and L. P. Gor'kov, *JETP* **12**, 1243 (1961).
- [53] P. Giannozzi, O. Andreussi, T. Brumme, O. Bunau, M. B. Nardelli, M. Calandra, R. Car, C. Cavazzoni, D. Ceresoli, M. Cococcioni *et al.*, *J. Phys.: Condens. Matter* **29**, 465901 (2017).
- [54] G. Pizzi, V. Vitale, R. Arita, S. Blügel, F. Freimuth, G. Géranton, M. Gibertini, D. Gresch, C. Johnson, T. Koretsune, J. Ibañez-Azpiroz, H. Lee, J.-M. Lihm, D. Marchand, A. Marrazzo, Y. Mokrousov, J. I. Mustafa, Y. Nohara, Y. Nomura, L. Paulatto, S. Poncè, J. Qiao *et al.*, *J. Phys.: Condens. Matter* **32**, 165902 (2020).
- [55] J. P. Perdew, K. Burke, and M. Ernzerhof, *Phys. Rev. Lett.* **77**, 3865 (1996).
- [56] D. Vanderbilt, *Phys. Rev. B* **41**, 7892 (1990).
- [57] A. Dal Corso, *Comput. Mater. Sci.* **95**, 337 (2014).
- [58] A. E. Böhrer, F. Hardy, F. Eilers, D. Ernst, P. Adelman, P. Schweiss, T. Wolf, and C. Meingast, *Phys. Rev. B* **87**, 180505(R) (2013).